

See discussions, stats, and author profiles for this publication at: <https://www.researchgate.net/publication/263962441>

Templated Biomineralization on Self-Assembled Protein Nanofibers Buried in Calcium Oxalate Raphides of Musa spp.

ARTICLE in CHEMISTRY OF MATERIALS · JUNE 2014

Impact Factor: 8.35 · DOI: 10.1021/cm501613w

CITATION

1

READS

46

8 AUTHORS, INCLUDING:



[Li Xiuli](#)

Huazhong Agricultural University

4 PUBLICATIONS 30 CITATIONS

[SEE PROFILE](#)



[Wenjun Zhang](#)

Huazhong Agricultural University

10 PUBLICATIONS 41 CITATIONS

[SEE PROFILE](#)



[Lijun Wang](#)

Huazhong Agricultural University

57 PUBLICATIONS 1,421 CITATIONS

[SEE PROFILE](#)

Templated Biomineralization on Self-Assembled Protein Nanofibers Buried in Calcium Oxalate Raphides of *Musa* spp.

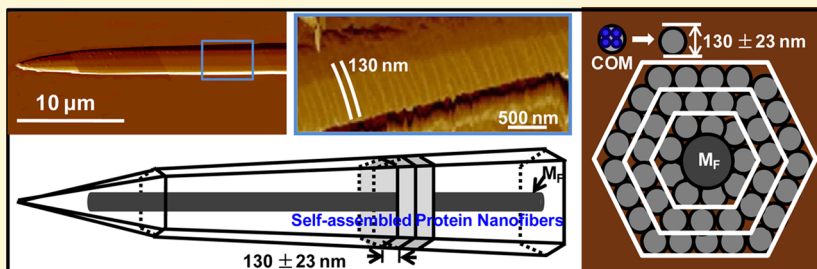
Xiuli Li,[†] Wenjun Zhang,[†] Jianwei Lu,[†] Lixue Huang,[†] Defeng Nan,[†] Mary Alice Webb,[‡] Francois Hillion,[§] and Lijun Wang^{*,†}

[†]College of Resources and Environment, Huazhong Agricultural University, Wuhan 430070, China

[‡]Department of Botany and Plant Pathology, Purdue University, West Lafayette, Indiana 47907, United States

[§]NanoSIMS Lab, Cameca, 92622 Gennevilliers, Cedex, France

S Supporting Information



ABSTRACT: Biological organisms possess an unparalleled ability to control crystallization of biominerals with convoluted internal structures. For example, an occluded organic matrix can interact with the mineral during its formation to control its morphology and structure. Although related matrix proteins that preferentially nucleate minerals have been identified, the mechanisms elucidating the structural and chemical complexity of calcium oxalate biominerals in plants remain unclear. Here, we show that a protein nanofiber (14 kDa) is embedded inside raphide (needle-shaped calcium oxalate) crystals of banana (*Musa* spp.), and that nanometer-scaled calcium oxalate spheres are arranged along the long axes of this central proteinaceous filament to form laminated structures through an aggregation-based growth mechanism, resulting in the final product of elongated and tapered hexagonal crystals. We further demonstrate that 11 amino acid peptide segments, with hydrophilic and hydrophobic residues rich in proline derived from the C-terminus of this full protein sequence, in vitro self-assemble into fibers and accelerate calcium oxalate nucleation kinetics. Remarkably, elongated and organized microstructures which are similar in appearance to natural raphide crystals are formed, emphasizing interactions between the mineral and self-assembled protein fibers. We anticipate that the present investigation of the structural and morphological complexity of plant calcium oxalate crystals and the underlying mechanisms of their formation will contribute to our understanding not only how plants evolved these sophisticated structures and morphologies for survival and adaptation, but also ultimately provide useful clues about how to maximally sequester calcium ions and/or oxalate in a confined compartment.

INTRODUCTION

Many biological organisms often control crystallization and morphology of minerals by producing an organic matrix that interacts with the mineral during its formation. Organic scaffolds in biominerals may comprise fibrous structural elements, for example, collagen in bone¹ or chitin in the chiton tooth.² In these systems, organic molecules provide templates to preferentially nucleate minerals and control their final structures and properties. Consequently, our understanding of biological control over mineral formation depends critically on characterizing the included organic–inorganic interfaces.²

Mineral formation is a widespread phenomenon in plants.³ In higher plants, calcium (Ca) oxalate is the most commonly formed mineral, occurring in most plant taxa. In addition some plant groups accumulate calcium carbonate (cystoliths) or amorphous silica (phytoliths).^{4–8} The formation of Ca oxalate crystals including calcium oxalate monohydrate (COM) is

considered to be a high-capacity mechanism for sequestering excess Ca in many plants. Ca oxalate precipitation typically occurs within specialized plant cells, called idioblasts, and it is clearly not a stochastic process, but appears to be controlled by specific biochemical and cellular mechanisms.⁹ These specialized cells and their associated molecules, collectively termed the organic matrix, function in a variety of ways to compartmentalize the crystallization process, to nucleate crystals, and to modify crystal growth and morphology.¹⁰ The complex cellular features associated with calcium oxalate crystallization indicate that it constitutes a biologically controlled process.¹¹

Plants produce calcium oxalate crystals in a variety of morphologies, and the crystal shape and location within the

Received: May 5, 2014

Published: May 29, 2014

plant is generally species-specific. In this study we have focused on needle-shaped, or acicular (about 150 μm in length and 4 μm in width) crystals called raphides in plants of *Musa* spp. (banana). Raphides typically form within idioblasts in organized bundles composed of hundreds of aligned crystals. Each individual raphide develops with a membrane compartment (so-called "crystal chambers") within the vacuole.^{9,11,12} All possible functions of these crystal chambers have likely not been established; however, it is clear that they play an important role in controlling crystal nucleation, growth and morphology;^{11,13} they mediate entry of ions and biomacromolecules such as proteins into the chambers, and they may also provide a barrier that prevents fusion of developing crystals within the vacuole.¹¹ Moreover, organic constituents such as calcium-binding proteins or self-assembled organic templates could also be present inside crystal chambers and involved in crystal nucleation or structure. Knowledge about the crystal chambers and any included organic constituents is essential for clarifying the mechanisms of calcium oxalate biominerization in plants.

Researchers have previously characterized components of the organic matrix that may influence crystal formation in plants. After demineralization of immature raphides in *Yucca brevifolia*, Arnott observed that an "organic structure" remained within the crystal chambers; however, the composition of that structure was not identified.¹² In another study, Webb et al. characterized the organic matrix associated with raphide idioblasts in grape and showed that this matrix could promote formation of raphide-like crystals.¹⁴ Bouropoulos et al. extracted macromolecules from crystals of tomato and tobacco and found that they promoted calcium oxalate nucleation and affected crystal growth in vitro.¹⁵ Li et al. extracted calcium oxalate from raphides in water lettuce (*Pistia stratiotes*) to reveal the organic matrix component and found that it was capable of in vitro precipitation of calcium oxalate to form the in vivo crystal morphology,¹⁶ suggesting that the organic matrix forms a template for such precipitation. Although a number of matrix proteins have been identified in plants, an understanding of their roles in the process of crystal development within cells is not entirely clear. In the present study, we have examined raphide idioblasts in plants of *Musa* spp. to identify matrix components associated with raphide formation. We have used a variety of methods, including high-spatial-resolution secondary ion microprobe spectrometry, in situ atomic force microscopy and protein analysis, to identify a protein included within the raphides. We suggest that this protein nanofiber could function in templating the formation of raphide crystals in banana.

■ EXPERIMENTAL SECTION

Isolation of Raphide Bundles. Mature pseudostems were washed with water and homogenized in ethanol for 5 min, and the resulting extract was filtered and washed with ethanol. The washing procedure, monitored with a dissecting microscope (Sunny, SZM45), separated raphide bundles from cell wall fragments and other contaminants. Isolated raphides were collected following dissolution of the bundles in distilled deionized water (>18 M Ω). Details of the isolation procedure are provided elsewhere.¹⁴

NanoSIMS. Raphides isolated from raphide bundles were fixed in 2.5% (v/v) glutaraldehyde and 2% (v/v) paraformaldehyde buffered with 50 mM PIPES (pH 7.2, 4 °C) for 12 h. The samples were postfixed for 2 h in 1% (v/v) osmium tetroxide buffered with 50 mM sodium cacodylate (pH 7.2) at room temperature. After fixation, the raphides were washed, dehydrated, and embedded in Spurr epoxy resin. Embedded samples were sectioned (0.5–1.0 μm in thickness)

using a rotary ultramicrotome (Leica RM2265) and deposited onto a droplet of water on Thermanox coverslips for nanoSIMS analysis. High-resolution SIMS analysis was performed using a CAMECA nanoSIMS 50L device. A focused 16-keV Cs⁺ primary ion beam was scanned over the surface of the sample, and the sputtered negative secondary ions were collected and analyzed using a double focusing mass spectrometer. Ion maps were collected simultaneously for ¹²C¹⁴N⁻, and ¹⁶O⁻. NanoSIMS maps are presented in an arbitrary linear color scale, with red and yellow regions indicating higher counts per second and blue and black regions indicating lower counts per second.

SDS-PAGE of Raphide Proteins. The purified raphide bundles (0.5 g) were washed thoroughly with deionized water (>18 M Ω), and the washed raphides were collected by centrifugation (10 000 rpm) for 10 min at 4 °C. The pelleted raphides were then boiled in 100 μL of 10% sodium dodecyl sulfate (SDS) in deionized water for 10 min, so-called SDS-soluble matrix protein¹⁴ and separated by SDS-polyacrylamide gel electrophoresis (SDS-PAGE). To extract internal proteins from the raphides, the pellet was boiled in 2 mL 10% SDS for 10 min, this repeated 5 times and then treated by acetone (4 °C, 24 h) to remove all surface proteins. The pellet was dissolved at 4 °C in ethylene diamine tetraacetic acid (EDTA) (0.16 M, pH 9.4) with a daily change of fresh EDTA until the volume of the insoluble materials was reduced by 95% (w/v). The insoluble materials were washed thoroughly with distilled water and then extracted with 78% (v/v) formic acid overnight at room temperature. The solution was clarified by centrifugation (4 °C, 10 000 rpm, 10 min), and the resulting supernatant containing formic acid-soluble matrix protein (M_F) was lyophilized. M_F was subsequently suspended in 5 M urea for further analysis¹⁶ and was separated by SDS-PAGE. Gels were prepared with a bis/acrylamide ratio of 0.8:30 (w/w) and an acrylamide concentration of 12.5% (w/v), and were stained with silver stain or coomassie brilliant blue.

Protein Identification by LTQ-ESI-MS/MS. Protein digestion by enzymes was performed according to the procedure of the filter-aided sample preparation (FASP) as described by Wiśniewski¹⁷ with some modifications. In brief, the protein pellet (about 30 μg) was solubilized in 30 μL SDT buffer (4% SDS, 100 mM DTT, 150 mM Tris-HCl at pH 8.0) for 5 min at 90 °C. Adding 200 μL UA buffer (8 M urea, 150 mM Tris-HCl at pH 8.0) to remove DTT, detergent and other low-molecular-weight components through repeated ultrafiltration (Microcon units, 30 kDa). Then, using 100 μL of 0.05 M iodoacetamide in UA buffer blocked reduced cysteine residues; the samples were incubated in darkness for 20 min. The filter was washed using 100 μL of UA buffer three times and 100 μL of 25 mM NH₄HCO₃ twice. Finally, the protein suspension was digested after addition of 2 μg of trypsin (Promega) in 40 μL of 25 mM NH₄HCO₃ at 37 °C for 12 h. Proteins were analyzed by an LTQ-ESI-MS/MS using a Finnigan LTQ mass spectrometer (Thermo Scientific) coupled with a Surveyor HPLC system (Thermo Scientific). Mass spectra were automatically searched using the Mascot version 2.2.04 search engine (Matrix Science, London, U.K.) and searching in the Expressed Sequence Tag (EST) of *Musa* database.¹⁸ Full methods and any associated materials can be found in the Supporting Information.

In Vitro Self-Assembly of Peptides and Mineralization. Peptide solutions were prepared by dissolution of the lyophilized 11-mer PRP peptide in 1.0 mM Tris buffer in the absence and presence of 0.52 mM CaCl₂ at pH 7.0 at concentrations of 0.1–1.0 mg/mL and stored at 4 °C prior to the experiments. The peptide samples were incubated (about 50 μL) with various substrates including freshly cleaved mica sheet, glass slides and TEM copper grids from 30 min to 3 h at room temperature, then the substrates were rinsed in distilled deionized water (>18 M Ω). For mineralization experiments, a selected substrate was incubated with peptides for 3 h, and then with a 50 μL supersaturated COM solution ($\sigma_{\text{COM}} = 1.3$) for 50 min to 2–3 h. The samples incubated in the peptides or supersaturated COM solutions were observed under AFM and SEM.

The relative supersaturation (σ) for COM crystallization is defined by $\sigma = [((\text{Ca}^{2+})(\text{C}_2\text{O}_4^{2-})) / K_{\text{sp}}]^{1/2} - 1$, where (Ca²⁺) and (C₂O₄²⁻) are the ionic activities calculated by successive approximation for the

ionic strength using the Davies extended form of the Debye–Hückel equation and mass balance expressions for total calcium and total oxalate with appropriate equilibrium constants. The solubility activity product, K_{sp} , of COM at room temperature (AFM studies) is $1.66 \times 10^{-9} \text{ mol}^2 \text{ L}^{-2}$.¹⁹

Synthetic COM Crystals for AFM Growth Studies. Clay (35.0 g) was added slowly to 300 mL of distilled deionized water ($>18 \text{ M}\Omega$) and stirred rapidly in a blender (Philips) until the gel became rigid enough. At this point, 20 g of NaCl was blended into the gel before each U tube was filled with 80 mL of gel. The tubes were tapped to get rid of air bubbles, and then filled with 0.5 M CaCl_2 and 0.5 M $\text{K}_2\text{C}_2\text{O}_4$ solution (molar ratio of $\text{Ca}^{2+}/\text{C}_2\text{O}_4^{2-} = 1$) at 62°C for 30 days. Harvested COM crystals were used for in situ AFM surface growth experiments.

For in situ AFM experiments, supersaturated $\text{CaC}_2\text{O}_4 \cdot \text{H}_2\text{O}$ solutions were prepared using $\text{K}_2\text{C}_2\text{O}_4 \cdot \text{H}_2\text{O}$ (Sigma-Aldrich, Guarantee Reagent, >99.5%) and CaCl_2 (Sigma-Aldrich, $\geq 96\%$). The ionic strength (I) was adjusted to 0.15 M by the addition of 1.50 M potassium chloride, and the solution pH 7.0 was maintained using 0.1 M, pH 7.0 tris(hydroxymethyl)aminomethane-HCl buffer. The PRP peptides (concentrations ranging from 100 to 600 nM) were added to a supersaturated solution ($\sigma = 0.508, 0.603, 0.712, \text{ or } 0.816$ with respect to COM). All in situ AFM experiments were carried out in a fluid cell on (101) or (010) surface of COM crystals.

COM Nucleation experiments were performed at a higher relative supersaturation, $\sigma_{\text{COM}} = 1.62$, $I = 0.15 \text{ M}$, pH 7.0, $25.0 \pm 0.1^\circ\text{C}$, and an ionic strength of 0.15 M, adjusted by the addition of sodium chloride. These nonseeded experiments were initiated by the slow mixing of solutions using a dosing device (876 Dosimat, Metrohm) to make the reaction solution supersaturated. All supersaturated solutions were prepared using reagent-grade chemicals (Sigma-Aldrich) and distilled deionized water ($>18 \text{ M}\Omega$). The peptide concentration used in nucleation studies was 100 nM of either PRP or BSA. Induction times are reported as mean \pm SD. COM nucleation was monitored by voltage changes using a potentiometer (Orion 720A, U.K.) incorporating a calcium ion selective electrode (9720 BNWP, ThermoScientific) and a reference electrode (Orion 900100). Crystals were collected periodically by centrifuge (8000g, 10 min at 25°C) and rinsed three times with distilled deionized water for SEM and XRD analysis.

In Situ AFM Imaging. All in situ COM growth and raphide dissolution experiments were performed in contact mode (Nanoscope V-Multimode 8, Bruker) on surfaces of natural or synthetic COM crystals anchored inside the enclosed fluid cell. AFM images were collected using Si_3N_4 tips (Bruker, tip model NP-S10) with spring constants of 0.35 N/m and 0.58 N/m. Details of the flow systems, image collection, and data analysis can be found in references.^{19,20} Typically, AFM tip convolution effects prevent accurate measurement of lateral dimensions below about 10 nm (or smaller than the diameter of an AFM tip). Because AFM height measurements do not suffer from tip convolution effects and are accurate to about 1 Å,²¹ we found that for globular particles or fibrous (cylindrical) structures, we could obtain good size (or diameter) estimates by measuring their heights.²¹

RESULTS

Raphides in banana (*Musa spp.*) form within crystal idioblasts that develop in the pseudostem of the plant (Figure 1A). Pseudostem is a stem-like structure composed of layered petioles of the leaves with the oldest petioles on the outside and progressively younger petioles, as well as curled leaf blades, to the interior (Supporting Information Figure S1). The shoot meristem is located inside the base of the pseudostem. Raphide idioblasts develop in large air spaces within the petiole on surfaces formed by parenchyma cells (Supporting Information Figure S1C, D) and on aerenchyma cells that bridge the air spaces (Supporting Information Figure S1E, F). The raphide idioblasts have a distinct elongated shape in contrast to the isodiametric parenchyma cells (Figure 1A). Figure 1B illustrates

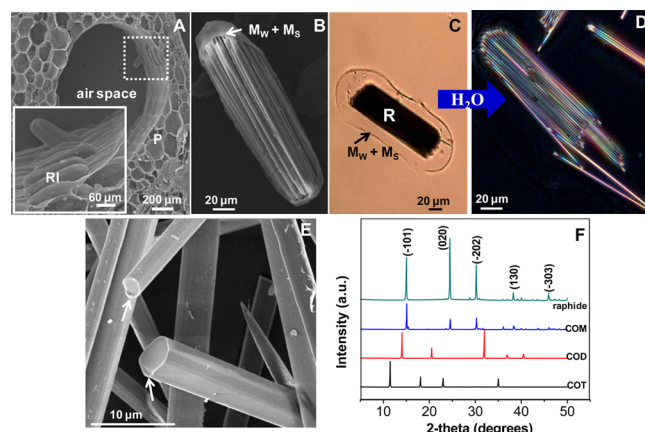


Figure 1. Morphology and structure of raphide idioblasts (RI) and isolated raphides (R) from pseudostem of banana (*Musa spp.*). (A) Cross section of pseudostem observed by SEM, indicating the position of raphide idioblasts along the surface of aerenchyma air space (indicated by a dotted rectangle and its enlargement (inset)). Raphide idioblasts are larger than surrounding parenchyma cells (P). (B) SEM and (C, D) optical images showing isolated raphide idioblasts enclosed by the water-soluble (M_W) and SDS-soluble (M_S) matrix indicated by the arrows in panels B and C. Following the addition of water, bundles of raphides disperse (D). (E) Individual raphides observed with SEM exhibit tapered hexagonal habits, and they are possibly covered by organic films as shown by the arrows in panel E. (F) X-ray diffraction patterns (XRD) show that the peaks corresponding to the raphide crystals isolated from banana match almost perfectly the standard peaks of COM, and do not match other phases of calcium oxalate crystals such as calcium oxalate dihydrate (COD) and calcium oxalate trihydrate (COT).

an isolated raphide bundle containing needle-shaped (acicular) raphide crystals (Figure 1D), which are embedded in a water- and sodium dodecyl sulfate (SDS)-soluble matrix (Figure 1C). After the matrix was removed examination of individual raphides with high-resolution field emission-SEM showed that they exhibit hexagonal or octahedral facets along their length and gradually taper at both ends of the crystal to form needle-like points (Figure 1E). Raphides extracted from the pseudostem were identified by X-ray diffraction (XRD) as COM (Figure 1F). To examine cross-sectional structure and composition individual raphide crystals were chemically fixed and embedded in resin and sectioned in 1 μm increments. Sections were subjected to in situ elemental microanalysis using secondary ion mass spectrometry (NanoSIMS) at a spatial resolution of ~ 50 nm. Figure 2A illustrates that an organic film is present in the outer layers of individual raphides, detected by NanoSIMS as $^{16}\text{O}^-$ and $^{12}\text{C}^{14}\text{N}^-$ secondary ions.

Raphides treated first with acetone and then etched in ethylene diamine tetraacetic acid (EDTA) solution were examined with in situ atomic force microscopy (AFM), which revealed a filamentous component that forms a double-stranded structure associated with the raphides (Figure 2D, E). AFM height images of partly demineralized raphide crystals show obvious fibrous structures with a height (diameter) of 9 ± 0.3 nm ($n = 10$, fibers) embedded in the individual raphide crystals (Supporting Information Figure S2B, C). The presence of protein fibers inside individual raphide crystals was supported by FTIR analysis of partially demineralized crystals (Figure 2F and Supporting Information Table S1), showing that absorption at $\sim 1630 \text{ cm}^{-1}$ was associated only with the raphide (Supporting Information Figure S3). The absorption feature is

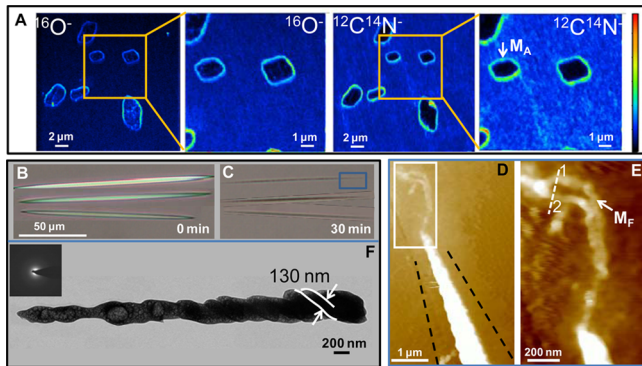
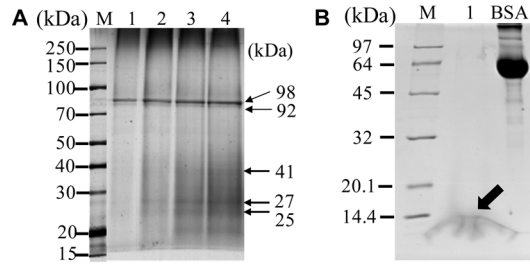


Figure 2. Organic matrix detections of individual raphides. (A) NanoSIMS images of the $^{16}\text{O}^-$ and $^{12}\text{C}^{14}\text{N}^+$ distribution of individual raphides, showing the outer layers of raphides with obvious organic components (M_A) that can be dissolved by acetone. Images of (B, C) polarized light microscopy (PLM) and (D, E) AFM of a partially EDTA-etched (for 30 min) single raphide pretreated with acetone (for 24 h) (imaged from a blue rectangle in (C)) revealing that raphide crystals are grown in a cylindrical fashion around a central proteinaceous filament, which is assembling in a double-stranded mode along the longitudinal axis of the raphide. (E) Enlargement of a rectangle in (D) showing two single chains (marked by 1 and 2) of a proteinaceous filament (M_F) as indicated by an arrow. (F) TEM image of a partially EDTA-etched single raphide demonstrating its self-assembled structure with a 130 nm-spacing marked by white curved lines. The SAED pattern (inset in panel F) shows the amorphous nature of the composite fiber.

well described for the amide I vibration mode, and it is characteristic of polypeptide- or protein-derived amino acids.²²

Matrix proteins were separated by sodium dodecyl sulfate polyacrylamide gel electrophoresis (SDS-PAGE) and then directly extracted from the gels (Figure 3A, B) for sequencing and potential identification. Protein from the fraction of matrix components (Figure 3A) (including the water-soluble (M_W), SDS-soluble (M_S), and part of acetone-soluble (M_A)) yielded obvious bands at about 98, 92, 41, 27, and 25 kDa. Protein (M_F) extracted by dissolution of the raphides produced a faint band with “edge tailing” at molecular mass of about 14 kDa (Figure 3B), suggesting that this protein correlated with the amide I of fibrous structures detected by in situ AFM and FTIR. Protein sequence (Figure 3C) was obtained by LTQ-ESI-MS/MS analysis (Supporting Information Figure S4). The gene encoding the protein closely matched nucleotide sequence in the banana genome for *Musa acuminata* AAA (Supporting Information Figure S4 and Tables S2–4). Calcium-binding amino acids, glutamate (E), aspartate (D), and cysteine (C),²³ comprise 16% of the total protein, and the carboxy terminus is rich in proline (P). BLAST analysis showed that the 14 kDa protein has a conserved DnaJ motif (Supporting Information Table S5). The amino acid sequence obtained from the 14 kDa band appears to comprise a complete sequence, and the entire sequence has a high degree of similarity with predicted protein sequences in a variety of plants.

We synthesized 11-mer proline-rich peptide (PRP) segments (Supporting Information Figures S5 and S6) derived from 101 to 111 of the C-terminus of the full-length protein sequence because it is highly conserved (Supporting Information Figure S7). After synthesis, 11-mer PRP peptide molecules at relatively high concentrations (800 nM to 8 μM) can spontaneously form fiber structures under different solution conditions. AFM images showed a network of fibers with a diameter of 1.0 \pm



C MENLTASEIA GFGVGALLLC ATIAAPRVDA FISASQRRLSL
DMCKRCGNLR MIACSQCKGI GSVRKGAFG FRVLEEIYES
LEDRNTPKQL VPCIKCQSKG RLPCPNCSKL P*

Figure 3. SDS–polyacrylamide gel electrophoresis image of idioblast and raphide protein extractions. (A) Replicate extractions from the idioblast organic fraction stained with silver. Lane 1–4 (22.0, 26.4, 33.0, or 39.6 μg of purified matrix proteins, respectively) shows SDS-soluble organic matrices including M_W , M_S , and part of M_A . (B) Extraction of the EDTA-insoluble organic matrix (3.0 μg) inside raphides stained with Coomassie. Purified raphides were pretreated with acetone for 24 h to remove all M_A and then dissolved in EDTA (0.16 M, pH 9.4). The EDTA-insoluble matrix was dissolved in 78% (v/v) formic acid (formic acid-soluble matrix, M_F), lyophilized, and finally dissolved in 5 M urea. The arrow indicates the 14-kDa band specifically bound to raphide. SDS-PAGE gels of (A, B) molecular weight markers and BSA are shown. (C) The deduced amino acid sequence was identified by LTQ-ESI-MS/MS analysis of the 14 kDa protein, and matched with nucleotide sequence in the banana genome (Supporting Information Figures S4 and S7). The marked sequence in red is the 11-mer PRP peptide.

0.2 nm ($n = 20$, fibers) (Figure 4C and Supporting Information Figure S8B, D) and lengths up to several micrometers (Figure 4A, B) to support that 11-mer peptides self-assemble into fibers. The peptide nanofibers were assembled and mineralized

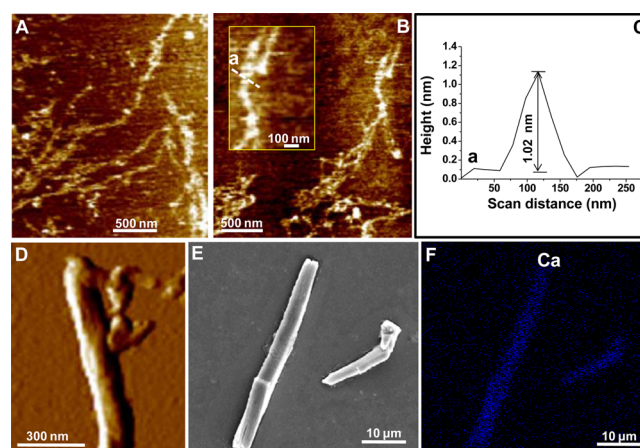


Figure 4. In vitro formation of self-assembled peptide fibers and mineralization. AFM images of 11-mer PRP peptides (800 nM to 8 μM) that self-assemble into fibers in 1.0 mM Tris buffer solution (pH 7.0) in the (A) absence and (B) presence of 0.52 mM CaCl_2 . The inset in panel B shows detail of the fiber, and (C) AFM height profile along a dotted line a in the inset reveals the height (diameter) of the fibers in their native hydrated state to be 1.0 ± 0.2 nm ($n = 20$, fibers) under experimental solution conditions in a fluid cell of AFM. (D) AFM image of fibers formed on a substrate incubated for 50 min in a supersaturated solution with respect to COM ($\sigma_{\text{COM}} = 1.3$). (E) SEM image of mature COM crystals after 2–3 h incubation and (F) SEM-EDS elemental map of Ca show that the peptide fibers are completely covered by Ca to form elongated COM crystals identified by XRD.

directly on substrates (mica or glass slides) in a supersaturated COM solution in an AFM fluid cell. After 50 min, the nanofibers became thick (Figure 4D) with a diameter up to >90 nm (Supporting Information Figure S9), and the fibers were covered with Ca throughout the surface of the fibers after 3 h. The mineral was analyzed by energy dispersive X-ray spectroscopy (EDS) (Figure 4F and Supporting Information Figure S10D), which revealed the formation of COM crystals along the fiber axis (Figure 4E and Supporting Information Figure S10A-C) identified by XRD (Supporting Information Figure S10F).

We also tested the effects of the low concentration 11-mer PRP peptide on induction times for in vitro COM nucleation. Nonseeded nucleation experiments were performed at a relative supersaturation, $\sigma_{\text{COM}} = 1.62$ and an ionic strength of 0.15 mol L^{-1} , and results showed significantly shorter induction times ($70 \pm 23 \text{ min}, n = 7$) in the presence of the PRP peptide segments at 100 nM than in control supersaturated solution without PRP ($99 \pm 7 \text{ min}, n = 3$) (Figure 5A and B). The addition of 100 nM of bovine serum albumin (BSA) to the supersaturated COM solutions slightly increased the induction times to $113 \pm 17 \text{ min}$ ($n = 3$), indicating that BSA had little

inhibition to no detectable effect on COM nucleation and morphology (Figure 5A, B and Supporting Information Figure S11B). COM crystallites nucleated in solutions with PRP exhibited considerably elongated morphology with length-to-width aspect ratio of $3.4\text{--}6.2$ (Supporting Information Figure S11C), compared to solutions without added PRP which had a ratio of about 2.6 (Supporting Information Figure S11A).

Quantitative determination of crystal growth rates at the near-molecular level were obtained by using *in situ* AFM to measure the $[101]$ and $[021]$ step velocity on $(\bar{1}01)$ and (010) faces, respectively (Figure 5C-F and Supporting Information Figures S12, S13). The $[101]$ or $[021]$ step velocity, determined through measurement of the step advance in successive images, was unchanged in the presence $100\text{--}300 \text{ nM}$ PRP segment (Figure 5G). No roughening of the $[101]$ or $[021]$ steps was observed, which is consistent with the absence of step pinning through adsorption of 11-mer PRP peptide at the $[101]$ and $[021]$ steps (Figure 5D, F). These results indicated that PRP peptide segments influence nucleation rather than growth of COM crystals.

To better understand the mechanisms of mineral formation and organization in banana raphides, we have conducted a series of demineralization experiments and directly imaged the individual raphide crystals by *in situ* AFM. The (100) -like surface of the hexagonal needle consists of regular bands (about 130 nm in width) aligned parallel to one another (Figure 6A), each consisting of calcium oxalate nanoparticles (53 to 76 nm , i.e., $65 \pm 12 \text{ nm}$ in diameter) (Figure 6B and Supporting Information Figure S14). Cross-sectional analyses of a fractured needle at the micrometer scale reveal that the needles have a lamellar structure, with layers of $105\text{--}124 \text{ nm}$ in thickness (Figure 6C), close to the bandwidth ($130 \pm 23 \text{ nm}$) (Figure 6A). Synthetic COM crystallites subjected to dissolution experiments in H_2O or EDTA solutions exhibited typical etch pits similar to growth hillocks on $(\bar{1}01)$ and (010) faces rather than nanoparticles (Supporting Information Figure S15), suggesting that these particulates could not be caused by sample preparation or etching artifacts. On the basis of the evidence observed in this study, we propose a model in which the protein fiber assemblies embedded in the core of raphide crystals control the arrangement of calcium oxalate nanoparticles into organized and elongated structures (Figure 6D and Supporting Information Figures S16, S17). In this model mineral nanoparticles assemble around the template of protein nanofibers into parallel arrays, and the nanoparticles fuse to form regular lamellar structures, leading to the final product of elongated and tapered crystallites.

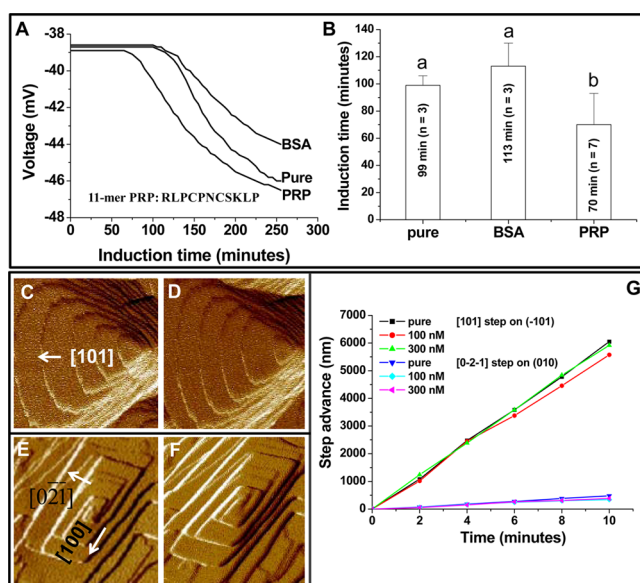


Figure 5. In vitro COM nucleation and growth in the absence and presence of 11-mer PRP. (A) Representative plots of voltage as a function of time for COM crystal nucleation ($\sigma_{\text{COM}} = 1.62$, $I = 0.15 \text{ M}$, pH 7.0, 25°C). A 100 nM 11-mer PRP segment dramatically accelerates the nucleation by decreasing the induction time. (B) Vertical error bars (the standard deviation of the mean) correspond to the variation in measured induction times. Different letters (a, b) show significant difference at $P \leq 0.05$. BSA (100 nM) served as a control. AFM images of growth hillocks on the (C, D) $(\bar{1}01)$ and (E, F) (010) face before and 60 min after addition of 300 nM 11-mer PRP, revealing the absence of the morphological changes of growth hillocks on both faces (σ_{COM} of 0.603 and 0.816 for $(\bar{1}01)$ and (010) face growth, respectively). (G) The step advance speed of the $[101]$ and $[021]$ steps, as measured from the center of the spiral dislocations during growth in solutions containing $100\text{--}300 \text{ nM}$ 11-mer PRP. The velocities of the $[101]$ and $[021]$ steps in the absence and presence of 11-mer peptide segment are $v_{0/i} = 9.8 \pm 0.4$ and $1.0 \pm 0.2 \text{ nm/s}$, respectively. Three independent sets of AFM experiments are presented for the velocity determination. Horizontal dimension: 900 nm (C, D) and 670 nm (E, F).

DISCUSSION

Although the exact relationship between full-length protein assemblies and formation of elongated minerals remains unresolved, our present findings suggest that COM biominerization in banana may rely on protein that preferentially nucleates minerals and controls their growth morphology. We have not fully characterized this unknown protein due to its trace amounts, however, sequence analysis indicated a putative conserved DnaJ domain in the protein. DnaJ, is a bacterial chaperone (Supporting Information Table S5) that is an ortholog of the cochaperone Hsp40 (heat shock protein) in eukaryotes, which functions in interaction with Hsp70. Previously, Webb et al. identified a cochaperone called Hip (Hsc70-interacting protein) as a raphide-associated protein in grape,²⁴ and it was later found that this protein contains a

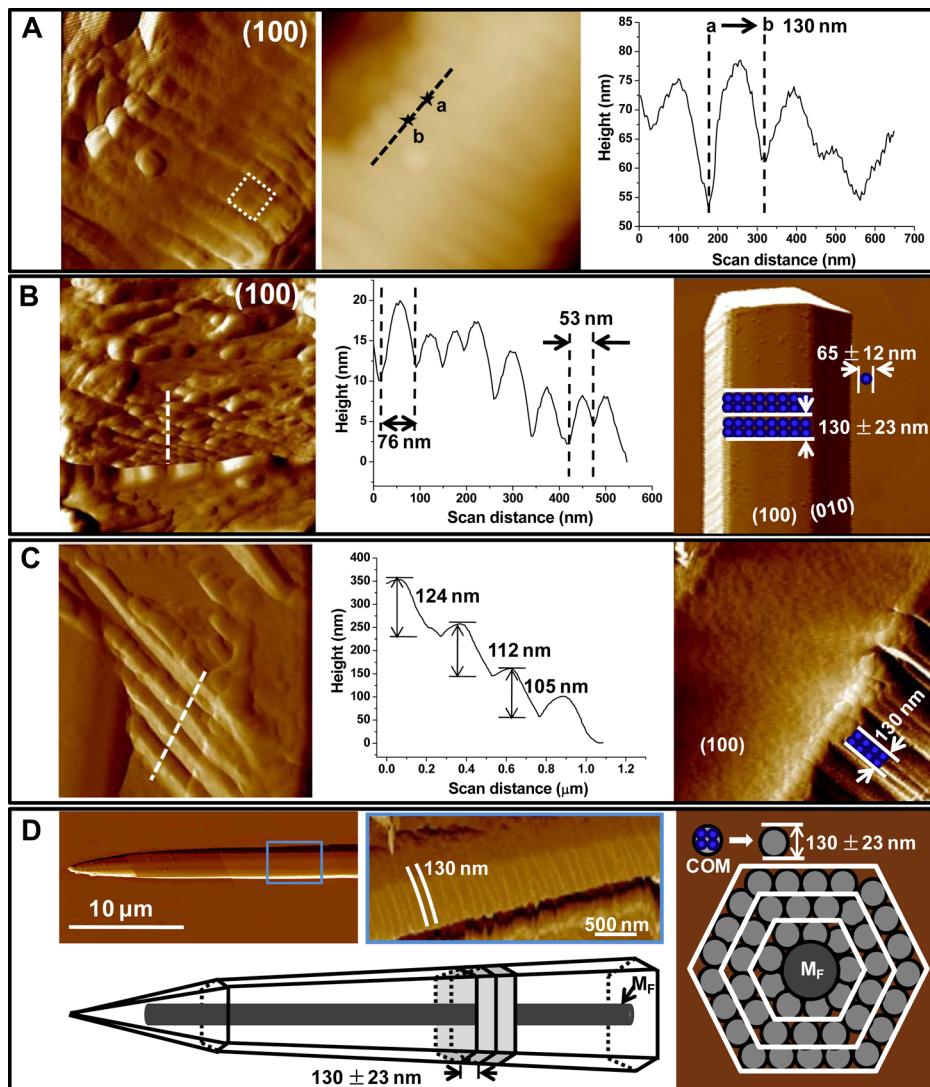


Figure 6. Structural analysis of the raphide crystals from *Musa* spp. (A) AFM deflection image (left) and the cross sectional analysis of the height of the regular bands (about 130 nm in width) along a dotted line on the (100)-like face in height image (middle). Horizontal dimension: 1.4 μ m. (B) Etching of the band revealing its consolidated nanoparticulate nature (65 ± 12 nm in horizontal dimension). Horizontal dimension: 2 (on the left) and 7.1 μ m (on the right). (C) AFM deflection images of a partially EDTA-etched needle (right, 2.2 μ m in horizontal dimension) and of a fractured needle (left, 2.3 μ m in horizontal dimension), and the cross-sectional analysis of this fractured needle (middle), revealing its lamellar structure (105–124 nm in thickness) based on its height image. (D) Proposed scheme summarizing the formation of individual COM needle-shaped crystals in the idioblast of *Musa* spp. Each 130 nm-nanoparticle is composed of four 65 nm-size nanoparticles as building blocks (indicated by a dotted rectangle in (A)), and they deposit around an axial filament (shown on the right) as core. These nanoparticles fuse to form the lamellar structures with width of about 130 nm (AFM image of enlargement of a blue rectangle in a partially etched raphide by EDTA (16 mM at pH 9.4 for 50 min)). The angle of the tapered hexagonal needles may be adjusted by the amount of Ca/oxalate uptake through reducing the number of the layers via a fixed distance/pitch from the middle to the tip of the needle (see Supporting Information Figures S16, S17 for details).

calcium-binding domain.²⁵ Identification of these two proteins suggest that molecular chaperones may play significant roles in raphide development. For example, entry of the matrix protein identified in this study into the crystal space may require cooperation with other chaperones such as Hip.²⁴ In plant cells, chaperone complexes including Tic40, which has some similarity to Hip, mediate transport of chloroplast proteins across the inner membrane and into the stroma.²⁶ In yeast mitochondria Hsp 70 interacts with a DnaJ protein (Jac1), and a scaffold protein (Isu) to assemble Fe/S clusters and transfer them to recipient proteins.²⁷

We selected a highly conserved 11-mer PRP segment derived from the C-terminal sequence of the full-length protein (Figure 3C and Supporting Information Figure S7). This segment

contains hydrophilic amino acids (Arg, Cys, Asn, Ser, and Lys) and hydrophobic amino acids (Leu and Pro). In this peptide segment, first, two Cys residues might form disulfide bonds, which may lock the supramolecular structure into place, thereby conferring a rigid 3D helical conformation.²⁸ Second, three proline amino acids are distributed within the C-terminal sequence. This is similar to the proline-rich amelogenin found in biological enamel,²⁹ which can stabilize mineral nanoclusters³⁰ and coassemble them into elongated crystals.³¹ The 11-mer PRP segment should create an amphiphile that assembles in solution into cylindrical micelles because of the amphiphile's overall conical shape.³² Self-assembly of a protein-amphiphile may be used in the banana raphide to make a nanostructured fibrous scaffold reminiscent of extracellular

matrix in bone. The fibers are able to direct mineralization of calcium oxalate through the promotion of nucleation rather than growth (Figure 5C–G) to form an elongated structure in which the crystallographic *c* axes of calcium oxalate are aligned with the long axes of the protein fibers (Supporting Information Figure S11). In addition, the change in induction time is not large (Figure 5A, B). Since induction time depends exponentially on the third power of the interfacial energy,³¹ the actual difference in interfacial energy is quite small. The real role of the fibers is to bind Ca (Figure 4F) and create an artificially high supersaturation at the peptide fiber-solution interface rather than to reduce interfacial energy. Furthermore, the band of this fiber protein (14 kDa) exhibited “edge tailing” (Figure 3B) because of solubility^{14,33} or glycosylation of the protein, which has two N/O-glycosylation sites within the PRP (Supporting Information Table S6 and Figure S6). Using fluorescent staining a previous study of *Musa* raphides detected a variety of organic substances associated with the raphides in the vacuole, and these could also potentially influence crystal formation.³⁴

Biominerals exhibit remarkable designs with building blocks that often are hierarchically arranged from the nanometer to the macroscopic length scales.³⁵ In our *in situ* AFM experiments, inorganic calcium oxalate nanocrystals (about 65 nm in diameter) may be the fundamental building blocks for the creation of highly ordered elongated solids along the protein fibers (Figure 6A and B). This is also similar to natural minerals that grow through such a mechanism of organized aggregation of nanocrystals.³⁶ It may be easy for an organism to repeatedly deposit nucleating particles. However, morphology does not define the crystallization pathway, that is, there are many possible pathways to get to a final morphology. It is unfortunately difficult to acquire high-resolution TEM evidence because of the beam-sensitivity of raphides when examined under the TEM at ambient temperatures¹⁵ to further support the calcium oxalate nanoparticles, their inner structure of these 65 nm nanoparticles and the origin of their precursors, and whether or not they are likely to be the nucleating particles as well. Using a focused ion beam in the dual beam SEM to prepare thin sections is also problematic, because the high energy ion beam may change the mineral crystallite phases during sample preparation. In the present study, we used AFM to image the exterior surface of etched and fractured raphides and clearly show that raphides in banana have a protein core and a complex nanoscale architecture that is composed of lamellae that appear to have a substructure of nanoparticles (Figure 6D). This fact implies that the orientation of crystalline nuclei and the subsequently growth are not random but are controlled by the self-assembled protein fibers. The exact mechanism of this control remains unclear; however, in similar systems, such control is gained by specific arrangement of charged amino acid residues³² that promote nucleation or growth of the crystals in a particular orientation. The simple needle-like morphology was a clear sign that the growth of these single raphides does not follow a classical mechanism with inhibitors. Given the recent findings of Habraken et al. about the ability of collagen to reduce the interfacial energy and promote nucleation,³⁷ as well as observations of Hamm et al. regarding self-assembled monolayers (SAMs),³⁸ it is also evident that even seemingly simple systems exploit this approach.

On the basis of the model we have proposed for raphide formation (Figure 6D), it is conceivable that the first level of

hierarchy is a biologically produced COM needle composed of consolidated nanospheres formed around a protein filament (M_F) (Figure 6D), and that the nanoparticles then fuse to form the regular lamellar structures (Figure 6C, D). In a further level of hierarchy, more than 200 needles in a specialized cell (idioblast) are arranged into parallel bundles (Figure 1B). The peptide segment used for *in vitro* self-assembly (Figure 4) and crystallization on peptide fibers (Figure 5 and Supporting Information Figure S11) in this study may have effects that differ from the full-length matrix protein, making direct translation of our results to *in vivo* raphide formation somewhat tenuous. However, this study has taken an important initial step toward a further understanding of an isolated factor, demonstrating that a peptide segment closely related to the full-length matrix protein controls COM nucleation and postnucleation growth at the earliest stages of mineralization. Hierarchical self-assembly of nanoparticles on the template of the protein fiber gives rise to a remarkably high degree of cooperativity (a state of greater interfacial structural match between inorganic and organic matrix nanophases).

CONCLUSIONS

The results from this plant biominerization system demonstrate that a self-assembled fiber inside of the raphide provides a template for the formation of COM needle-shaped minerals in a confined space (crystal chamber). The complex interactions between the fiber and mineral nanoparticles control the deposition and final structure of the mineral. The fiber biochemistry and self-assembly that could influence where and when nucleation of the mineral phase occurs deserves a separate study. Further study of the structural and morphological complexity of plant COM crystals and the underlying mechanisms of their formation will contribute to our understanding about how plants evolved these sophisticated structures for survival and adaptation. In addition, examination of COM mineralization in plants could contribute to knowledge about how calcium ions and/or oxalate in confined compartments are sequestered during human pathological mineralization (i.e., stone formation).

ASSOCIATED CONTENT

S Supporting Information

(1) Methods in detail, (2) the EST sequence and blast results (Tables S2–S5), (3) distribution of raphide idioblasts (RIs) in banana pseudostem (Figure S1), (4) AFM, FTIR, and LTQ-ESI-MS/MS analysis for 14 kDa unknown protein (Figures S2–4, S7; Table S1), (5) structure of synthesized 11-mer peptide segment (Figures S5, S6; Table S6), (6) *in vitro* formation of self-assembled 11-mer peptide fibers (Figures S8–S10), (7) AFM images of COM growth in the presence of 11-mer peptide in various supersaturated solutions (Figures S12, S13, S15), and (8) structural analysis inside of needle-shaped raphide crystals (Figures S14, S16, S17). This material is available free of charge via the Internet at <http://pubs.acs.org>.

AUTHOR INFORMATION

Corresponding Author

*E-mail: lqwang@mail.hzau.edu.cn.

Notes

The authors declare no competing financial interest.

■ ACKNOWLEDGMENTS

We would like to thank Dr. James DeYoreo for constructive suggestions. We also thank Dr. Richard Gordon for careful reading of the manuscript. This work was supported in part by a grant (No. 31301841) from the National Natural Science Foundation of China (to W.J.Z.), a Specialized Research Fund for the Doctoral Program of Higher Education (20130146110030), a startup grant (2010BQ063), and the Fundamental Research Funds for the Central Universities (2012MBDX014) from the Huazhong Agricultural University (to L.J.W.). J.W.L. acknowledges a grant (No. IRT1247) from the program for Changjiang scholars and innovative research team in university of China. M.A.W. acknowledges research support from Hatch Act funds provided by the U.S. Department of Agriculture.

■ REFERENCES

- (1) Weiner, S.; Wagner, H. D. *Annu. Rev. Mater. Res.* **1998**, *28*, 271–298.
- (2) Gordon, L. M.; Joester, D. *Nature* **2011**, *469*, 194–197.
- (3) Lowenstam, H. A.; Weiner, S. *On Biomineralization*; Oxford University Press: New York, 1989.
- (4) Neethirajan, S.; Godron, R.; Wang, L. J. *Trends Biotechnol.* **2009**, *27*, 461–467.
- (5) Bauer, P.; Elbaum, R.; Weiss, I. M. *Plant Sci.* **2011**, *180*, 746–756.
- (6) He, H.; Bleby, T. M.; Veneklaas, E. J.; Lambers, H.; Kuo, J. *Ann. Bot.* **2012**, *109*, 887–896.
- (7) Gal, A.; Hirsch, A.; Siegel, S.; Li, C.; Aichmayer, B.; Politi, Y.; Fratzl, P.; Weiner, S.; Addadi, L. *Chem.—Eur. J.* **2012**, *18*, 10262–10270.
- (8) Nakata, P. *Front. Biol.* **2012**, *7*, 254–266.
- (9) Franceschi, V. R.; Nakata, P. *Annu. Rev. Plant Biol.* **2005**, *56*, 41–71.
- (10) Weiner, S.; Addadi, L. *Annu. Rev. Mater. Res.* **2011**, *41*, 21–40.
- (11) Webb, M. A. *Plant Cell* **1999**, *11*, 751–761.
- (12) Arnott, H. J.; Pautard, F. G. E. Calcification in plants. *Biological Calcification: Cellular and Molecular Aspects*; Schraer, H., Ed.; Appleton-Century-Crofts: New York, 1970; pp 375–446.
- (13) Simkiss, K.; Wilbur, K. M. *Biomineralization: Cell Biology and Mineral Deposition*; Academic Press: San Diego, CA, 1989.
- (14) Webb, M. A.; Cavaletto, J. M.; Carpita, N. C.; Lopez, L. E.; Arnott, H. J. *Plant J.* **1995**, *7*, 633–648.
- (15) Bouropoulos, N.; Weiner, S.; Addadi, L. *Chem.—Eur. J.* **2001**, *7*, 1881–1888.
- (16) Li, X.; Zhang, D.; Lynch-Holm, V. J.; Okita, T. W.; Franceschi, V. R. *Plant Physiol.* **2003**, *133*, 549–559.
- (17) Wiśniewski, J. R.; Zougman, A.; Nagaraj, N.; Mann, M. *Nat. Methods* **2009**, *6*, 359–362.
- (18) D'Hont, A.; Denoeud, F.; Aury, J. M.; Baurens, F. C.; Carreel, F.; Garsmeur, O.; Noel, B.; Bocs, S.; Droc, G.; Rouard, M.; Da Silva, C.; Jabbari, K.; Cardi, C.; Poulain, J.; Souquet, M.; Labadie, K.; Jourda, C.; Lengellé, J.; Rodier-Goud, M.; Alberti, A.; Bernard, M.; Correa, M.; Ayyampalayam, S.; Mckain, M. R.; Leebens-Mack, J.; Burgess, D.; Freeling, M.; Mbégué-A-Mbégué, D.; Chabannes, M.; Wicker, T.; Panaud, O.; Barbosa, J.; Hribova, E.; Heslop-Harrison, P.; Habas, R.; Rivallan, R.; Francois, P.; Poiron, C.; Kilian, A.; Burthia, D.; Jenny, C.; Bakry, F.; Brown, S.; Guignon, V.; Kema, G.; Dita, M.; Waalwijk, C.; Joseph, S.; Dievart, A.; Jaillon, O.; Leclercq, J.; Argout, X.; Lyons, E.; Almeida, A.; Jeridi, M.; Dolezel, J.; Roux, N.; Risterucci, A. M.; Weissenbach, J.; Ruiz, M.; Glaszmann, J. C.; Quétier, F.; Yahiaoui, N.; Wincker, P. *Nature* **2012**, *488*, 213–217.
- (19) Wang, L. J.; Qiu, S.; Zachowicz, W.; Guan, X. Y.; De Yoreo, J. J.; Nancollas, G. H.; Hoyer, J. R. *Langmuir* **2006**, *22*, 7279–7285.
- (20) Qiu, S. R.; Wierzbicki, A.; Salter, E. A.; Zepeda, S.; Orme, C. A.; Hoyer, J. R.; Nancollas, G. H.; Cody, A. M.; De Yoreo, J. J. *J. Am. Chem. Soc.* **2005**, *127*, 9036–9044.
- (21) Cho, K. R.; Huang, Y.; Yu, S.; Yin, S.; Plomp, M.; Qiu, S. R.; Lakshminarayanan, R.; Moradian-Oldak, J.; Sy, M. S.; De Yoreo, J. J. *J. Am. Chem. Soc.* **2011**, *133*, 8586–8593.
- (22) Mantsch, H. H.; Chapman, D. *Infrared Spectroscopy of Biomolecules*; Wiley-Liss: New York, 1996.
- (23) Ho, Y. P.; Yang, M. W.; Chen, L. T.; Yang, Y. C. *Mass Spectrom.* **2007**, *21*, 1083–1089.
- (24) Webb, M. A.; Cavaletto, J. M.; Klanrit, P.; Thompson, G. A. *Cell Stress Chaperones* **2001**, *6*, 247–255.
- (25) Klanrit, P. Functional characterization of Hsc 70 Interacting protein (Hip) and chaperone interactions in *Vitis labrusca* and *Arabidopsis thaliana*. PhD thesis, Purdue University, West Lafayette, IN, 2006.
- (26) Chou, M. L.; Fitzpatrick, L. M.; Tu, S. L.; Budziszewski, G.; Potter-Lewis, S.; Akita, M.; Levin, J. Z.; Keegstra, K.; Li, H. M. *EMBO J.* **2003**, *22*, 2970–2980.
- (27) Majewska, J.; Ciesielski, S. J.; Schilke, B.; Kominek, J.; Blenska, A.; Delewski, W.; Song, J. Y.; Marszalek, J.; Craig, E. A.; Dutkiewicz, R. *J. Biol. Chem.* **2013**, *288*, 29134–29142.
- (28) Suzuki, M.; Saruwatari, K.; Koqure, T.; Yamamoto, Y.; Nishimura, T.; Kato, T.; Nagasawa, H. *Science* **2009**, *325*, 1388–1390.
- (29) Friddle, R.; Battle, K.; Trubetskoy, V.; Tao, J.; Salter, E. A.; Moradian-Oldak, J.; De Yoreo, J. J.; Wierzbicki, A. *Angew. Chem., Int. Ed.* **2011**, *50*, 7541–7545.
- (30) Du, C.; Falini, G.; Fermani, S.; Abbott, C.; Moradian-Oldak, J. *Science* **2005**, *307*, 1450–1454.
- (31) Wang, L. J.; Guan, X. Y.; Du, C.; Moradian-Oldak, J.; Nancollas, G. H. *J. Phys. Chem. C* **2007**, *111*, 6398–6404.
- (32) Hartgerink, J. D.; Beniash, E.; Stupp, S. I. *Science* **2001**, *294*, 1684–1688.
- (33) Kubo, K. *Anal. Biochem.* **1993**, *213*, 200–205.
- (34) Bruni, A.; Dallolio, G.; Tosi, B. *New Phytol.* **1982**, *92*, 581–587.
- (35) Aizenberg, J.; Weaver, J. C.; Thanawala, M. S.; Sundar, V. C.; Morse, D. E.; Fratzl, P. *Science* **2005**, *309*, 275–278.
- (36) Banfield, J. F.; Welch, S. A.; Zhang, H.; Ebert, T. T.; Penn, R. L. *Science* **2000**, *289*, 751–754.
- (37) Habraken, W. J. E. M.; Tao, J.; Brylka, L. J.; Friedrich, H.; Bertinetti, L.; Schenk, A. S.; Verch, A.; Dmitrovic, V.; Bomans, P. H.; Frederik, P. M.; Laven, J.; van der Schoot, P.; Aichmayer, B.; de With, G.; De Yoreo, J. J.; Sommerdijk, N. A. *Nature Comm.* **2013**, *4*, 1507 DOI: 10.1038/ncomms2490.
- (38) Hamm, L. M.; Giuffre, A. J.; Nan, N.; Tao, J.; Wang, D.; De Yoreo, J. J.; Dove, P. M. *Proc. Natl. Acad. Sci. U.S.A.* **2014**, *111*, 1304–1309.